Arabian Journal of Chemistry (2023) **16**, 104797

King Saud University

Arabian Journal of Chemistry

www.ksu.edu.sa
www.sciencedirect.com

ORIGINAL ARTICLE

Efficient one-pot synthesis of antimony-containing mesoporous tin dioxide nanostructures for gas-sensing applications

Tariq Aqeel [a,*], **Vardan Galstyan** [b,c], **Elisabetta Comini** [b], **Ali Bumajdad** [d]

[a] *Department of Science, College of Basic Education, The Public Authority of Applied Education and Training (PAAET), P.O. Box 23167, Safat 13092, Kuwait*
[b] *Sensor Lab, Department of Information Engineering, University of Brescia and ISTM, Via Valotti 9, 25133 Brescia, Italy*
[c] *Department of Engineering "Enzo Ferrari", University of Modena and Reggio Emilia, Via Vivarelli 10, 41125 Modena, Italy*
[d] *Department of Chemistry, Faculty of Science, Kuwait University, P.O. Box 5969, Safat 13060, Kuwait*

Received 16 November 2022; accepted 8 March 2023
Available online 15 March 2023

KEYWORDS

Mesoporous nanomaterial;
Antimony doping;
Tin dioxide;
Nitrogen dioxide;
Acetone;
Gas sensor

Abstract Currently, wide-bandgap metal oxide nanomaterials with attractive chemical and physical properties are intensively used for the fabrication of chemiresistive gas sensors and other catalytic devices. However, the low electrical conductance of sensors based on wide bandgap metal oxides is an issue that limits their application in small-scale systems to read out electrical signals and the manufacturing of portable sensing devices. In this regard, combining oxide nanostructures with other elements could be an effective strategy for enhancing their electrical and sensing performances. In this work, we attempted to improve the conductivity and sensitivity of porous tin dioxide to certain gases. Herein, we report a cost-effective and simple method for synthesizing antimony-containing mesoporous tin dioxide (Sb-SnO_2) under ambient pressure and temperature. The X-ray diffraction, N_2 sorption, transmission electron microscopy, energy-dispersive X-ray, and photoelectron spectroscopy analyses indicate that the prepared Sb-SnO_2 material is a nanocrystalline powder with a large surface area. Meanwhile, the successful incorporation of Sb into the SnO_2 framework results in increased electrical conductance by at least one order of magnitude or more compared to that of pure SnO_2 and other doped SnO_2 materials, respectively. The structure shows a very effective sensing response to volatile organic compounds and nitrogen dioxide. Hence, we developed an efficient method for synthesizing highly conductive oxide nanomaterials for use in chemical gas sensing devices.

---

[*] Corresponding author.
E-mail address: tm.aqeel@paaet.edu.kw (T. Aqeel).

Peer review under responsibility of King Saud University.

ELSEVIER **Production and hosting by Elsevier**

https://doi.org/10.1016/j.arabjc.2023.104797

1. Introduction

Tin dioxide is an *n*-type semiconductor material with a band gap of 3.6 eV (Aswaghosh et al., 2016; Popescu et al., 2001; Shaalan et al., 2016). It is widely employed in different fields, including chemical gas sensing devices (Benhebal et al., 2011; Brunet et al., 2012; Chen et al., 2013; Das et al., 2017; Li et al., 2012; Wagner et al., 2011) and optical detectors (Ganose and Scanlon, 2016; Huang et al., 2014; Suh et al., 2021; Yu et al., 2011). This is mainly due to its relatively low cost, excellent chemical stability, and fast charge transfer (Chowdhury and Bhowmik, 2021; Ponja et al., 2018; Wang et al., 2021). Tailoring the surface chemistry or the morphology of SnO_2 affects its band gap (Chakraborty et al., 2021), and eventually its reactivity toward different gaseous compounds. Furthermore, the band gap of semiconducting materials can be affected by many factors, such as doping with other elements (Ganose and Scanlon, 2016; Morris et al., 2001; Noor and Parkin, 2013; Shokr et al., 2000; Terrier et al., 1997; Yu et al., 2011), the formation of structural defects (Morris et al., 2001), and the modification of their crystallite size (Brus, 1984; Manikandan et al., 2016; Masuda, 2022). Moreover, the synthesis of semiconductor materials with porous morphology considerably increases the surface area of these materials, which is crucial to improving their interaction with gaseous and volatile organic compounds (VOCs) (Chowdhury and Bhowmik, 2021; Martinez et al., 2005; Masuda, 2022). The surface area of non-porous SnO_2 (Smith and Nie, 2011) could be increased from 10 $m^2\ g^{-1}$ to form mesoporous SnO_2 of approximately 200 $m^2\ g^{-1}$ (Goebbert et al., 1999). The surface area of oxide materials can also be affected by different treatment parameters employed during their calcination (Chen and Cao, 2020; Goebbert et al., 1999; Koo et al., 2017). In addition, heat treatment can affect the crystallite sizes of SnO_2 (Goebbert et al., 1999; Noor and Parkin, 2013; Oakton et al., 2016; Zhong et al., 2012). It was found that SnO_2 with an increased surface area and reduced crystallite size shows improved surface redox reactions and adsorption/desorption properties, thus leading to enhanced sensitivity of SnO_2 toward low gas concentrations (Yamazoe et al., 2003; Masuda, 2022). Moreover, the formation of a framework with interconnected crystallites improves the overall charge transfer in the material, which is beneficial for its sensing response (Aegerter et al., 1997; Noor and Parkin, 2013; Shao et al., 2016).

Further, the introduction of different elements into the SnO_2 framework may improve its electrical conductance (Terrier et al., 1997; Zhong et al., 2012) as well as its sensing properties by increasing the surface charge (Chakraborty et al., 2021; Yamazoe et al., 2003). In antimony-doped SnO_2, Sb atoms replace Sn atoms in the framework (Zhong et al., 2012), introducing more electrons to the conduction band and generating more structural defects, such as oxygen vacancies (Brus, 1984; Manikandan et al., 2016; Zhong et al., 2012), owing to the higher oxidation state of Sb (Kojima et al., 1997; Terrier et al., 1997). As a result, an additional "defect band" is introduced beneath the main conduction band (Chowdhury and Bhowmik, 2021; Kojima et al., 1997), thus lowering the main band gap of the material and facilitating the transport of more valence electrons at lower energies (Ganose and Scanlon, 2016; Smith and Nie, 2011; Yu et al., 2011). Thus, decreasing the band gap of SnO_2 from 3.6 eV to $\sim$ 3 eV reduces the heating energy required to conduct electricity, leading to a lower operating temperature of the material.

In general, mesoporous SnO_2 powders are directly synthesized using solvothermal (hydrothermal), precipitation, and self-templating methods. The self-templating method relies solely on the thermal decomposition of organic ligands attached to the metal in a metal–organic framework in the presence of air. This will convert the organic ligands into gas and the metal into porous crystalline metal oxides (Wang et al., 2021). The solvothermal method, which employs heat treatment of the reaction mixture in a sealed container under internal pressure, was first used to produce mesoporous SnO_2 by Chen and Liu (1999). Later, this method was used to prepare SnO_2 containing different elements such as F-, Sb-, and In-doped SnO_2 (Hao et al., 2014; Oh et al., 2015; Shao et al., 2016). In contrast, SnO_2 precipitation occurs in a reaction vessel at atmospheric pressure and was first reported to produce mesoporous SnO_2 by Severin and Abdel-Fattah (1998). However, the prepared porous product collapsed during calcination above 350 °C, which could explain the subsequent rare use of this method. We previously reported a highly reproducible method of synthesizing SnO_2 based on the modified Severin's precipitation synthesis, where the mesoporous SnO_2 endured multiple heat treatments up to 500 °C (Aqeel et al., 2016). Our improved method produced crystalline mesoporous SnO_2 powders containing a wide range of elements. In this study, we employed the aforementioned modified method to synthesize a mesoporous crystalline Sb-containing SnO_2 (Sb-SnO_2) powder with a large surface area and small crystallite size. The modified structural, morphological, and compositional properties of our Sb-SnO_2 material resulted in improved electrical conductivity and sensing performance.

2. Materials and methods

2.1. *Chemicals*

Hexadecylamine (90%), iPrOH (99%), $Sn(OiPr)_4$ (99%), and $SbCl_3$ (99%) were purchased from Alfa Aesar. Ethanol (99.8%) was obtained from Sigma-Aldrich. All chemicals were used without further purification.

2.2. *Synthesis of mesoporous Sb–SnO_2*

To prepare a mesoporous Sb-SnO_2 powder, first, hexadecylamine (0.28 g) was dissolved in isopropyl alcohol (24.4 mL), followed by the addition of $Sn(OiPr)_4$ (1.9 g) and $SbCl_3$ (0.1 g) with continuous stirring at 25 °C. The reaction mixture was slowly stirred in humid air (approximately 80% humidity) at atmospheric pressure and room temperature for 3 d. The precipitated product was filtered and washed with water and ethanol. The surfactant was extracted from the product with ethanol using a Soxhlet extractor overnight (approximately 16 h), and the product was subsequently filtered. Finally, the product was calcined at 300 °C in air for 1 h and then at 400 °C for 15 min (heating rate of 2 °C min^{-1}). The obtained material was denoted as Sb-SnO_2.

2.3. *Material characterization techniques*

The synthesized powder was analyzed using X-ray diffraction (XRD), high-resolution transmission electron microscopy (HRTEM), energy-dispersive X-ray (EDX), and X-ray photoelectron spectroscopy (XPS). XRD measurements were performed using a Bruker AXS D8 ADVANCE diffractometer equipped with a copper target (λ = 1.5418 Å). The DIFFRAC^{plus} software was used for the analyses, and the operational parameters were set as follows: 40 kV, 40 mA, 0.1 mm low-angle front slit window size, 1.0 mm for wide-angle scans, 0.5–1.0 mm between the deflection plate and the sample for low-angle scans, and 0.5 steps s^{-1} in continuous coupled two-theta/theta scan modes. A Micromeritics TriStar analyzer was used for nitrogen gas adsorption–desorption analyses. A JEOL JEM-2011 microscope was utilized to obtain HRTEM images at an operating voltage of 200 kV. The TEM images were captured and analyzed using a Gatan 794 CCD camera and ImageJ software, respectively. The Oxford Link ISIS Semi STEM EDX system equipped with the TEM system was used to determine sample chemical compositions. XPS spectra were obtained using a Thermo Fisher Scientific ESCALAB 250Xi spectrometer equipped with a monochromator and an Al-Kα radiation source (1486.6 eV), and an Avantage data system was employed for spectral recording and processing. The XPS measurement parameters were set as follows: 10^{-9} Torr analysis chamber pressure, 0.1 eV step size, 100 ms dwell time, and 20 eV pass energy. The C 1 s line (284.6 eV) of adventitious carbon was used to determine binding energy values. A flood gun was used to neutralize charge buildup on the surface of the insulating layer in the standard charge compensation mode.

The gas-sensing tests of the materials prepared in this study were performed as follows: Interdigitated platinum electrodes and a heater were deposited on the surface and backside of the alumina substrate using radio frequency (RF) magnetron sputtering. Next, a 0.14 mg mL^{-1} dispersion of the Sb-SnO_2 powder in ethanol was dropped on the substrate. Subsequently, thermal treatment of the fabricated sensing structure (Scheme 1) was performed in air at 200 °C for 1 h.

The sensing properties of the material toward nitrogen dioxide, acetone, ethanol, and hydrogen were investigated in a test chamber using a flow-through technique. The humidity level in the test chamber was set at 40%. Each analyte gas was injected into the chamber at the desired concentration. After each measurement, the test chamber was purified with synthetic air.

3. Results and discussion

3.1. XRD patterns

The small-angle XRD pattern presented in Fig. 1 (a) shows a main diffraction peak corresponding to the (1 0 0) plane of Sb–SnO_2, indicating its mesoporous structure. The absence of other peaks indicates that the pores show no long-range order (wormhole-like pores). Moreover, the shape of the main diffraction peak indicates that Sb is well-incorporated into the framework and does not damage the overall pore ordering in the structure (Du et al., 2012; Goebbert et al., 1999; Ponja et al., 2018). As shown in Fig. 1 (b), the wide-angle XRD pattern of Sb–SnO_2 confirms its crystalline nature, with only one phase of synthesized SnO_2 (Wang et al., 2009). The diffraction peaks can be assigned to the cassiterite (tetragonal) structure of SnO_2 (Das et al., 2014; Du et al., 2012; Goebbert et al., 1999; Liu et al., 2012; Müller et al., 2011; Noor et al., 2015; Oh et al., 2015; Shao et al., 2016; Zhong et al., 2012). No additional diffraction peaks were observed that could be attributed to the formation of Sb_xO_y clusters outside the framework. This result also confirms that the substitution of Sb ions does not affect the crystallinity of SnO_2 (Oakton et al., 2016; Wang et al., 2009) and Sb ions inserted into the framework (Liu et al., 2012). This is expected because the ionic radius of Sb^{5+} (0.6 Å) is similar to that of Sn^{4+} (0.69 Å) (Ponja et al., 2018). Moreover, the average crystallite size was calculated to be 3.5 nm from the full width at half maximum of the (1 1 0) diffraction peak using the Scherrer equation.

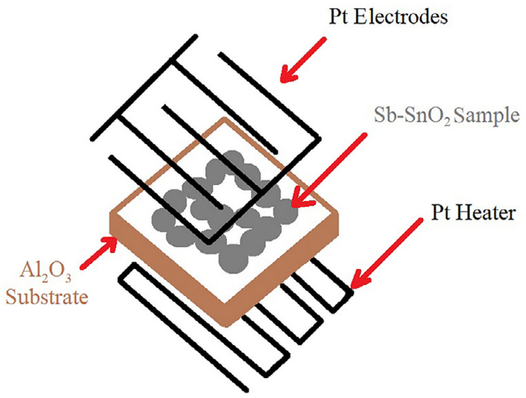

Scheme 1 Schematic of the sample for gas sensing measurements.

3.2. XPS spectra

Fig. 2 shows the XPS spectra of the prepared Sb-SnO_2 nanomaterial. The binding energies of Sn spin coupling of the 3d orbitals at 486.6 and 495.0 eV exhibit a 3d orbit-splitting shift of 8.4 eV. This corresponds to the Sn^{4+} oxidation state of SnO_2 (Hao et al., 2014; Wang et al., 2009; Feng et al., 2022). As shown in Fig. 2 (b), the Sb $3d_5$ peak overlaps with the O 1 s peak. After deconvolution of the asymmetric peak, the O 1 s peak at 530.6 eV could be ascribed to the O^{2-} species in the SnO_2 lattice (Hao et al., 2014), and the other peak at 531.8 eV to the Sb $3d_5$ peak. The Sb $3d_3$ peak is well resolved at 540.0 eV, and its position and symmetrical shape correspond to Sb^{5+} in Sb_2O_5 (Hou et al., 2009; Nag et al., 2014; Wang et al., 2009). This is in line with the wide-angle XRD results discussed in Section 3.1. Both Sb peaks confirm the successful substitution of Sb^{5+} in the SnO_2 framework (Ponja et al., 2018). Based on the XPS data, the Sb content incorporated into SnO_2 was calculated to be 5 wt%, which is close to the amount of Sb added during Sb–SnO_2 synthesis (6 wt%).

3.3. N_2 Sorption analysis

The N_2 sorption analysis was performed for Sb–SnO_2 powder and the obtained isotherm curve can be ascribed to the Type I (b) isotherm (Thommes et al., 2015), which is typical for materials with wide micropores and narrow mesopores (Fig. 3 (a)). The shape of this isotherm is generally flat in the relative pressure range of 0.4–0.8, indicating the complete monolayer adsorption of N_2. In addition, the sample showed no hysteresis between adsorption and desorption cycles, indicating a narrow pore size distribution (∼25 Å) and no cylindrical pores (absence of capillary condensation). Moreover, the Brunauer–Emmett–Teller (BET) surface area of the sample was determined to be 155 m^2 g^{-1} with an average pore size of 22 Å (Fig. 3 (b)). The results obtained from the isotherm and pore size distribution confirm the successful synthesis of mesoporous Sb–SnO_2 material according to IUPAC (Thommes et al., 2015).

3.4. TEM analysis

TEM images in Fig. 4 (a) reveal and confirm the presence of wormhole-like pores without the long-range order throughout the Sb–SnO_2 material, as previously demonstrated by the small-angle XRD results in Section 3.1. Based on the HRTEM image of the sample in Fig. 4 (b), the d spacing of 0.33 nm corresponds to the crystalline (1 1 0) plane of SnO_2. In addition, the sample contains aggregated spherical crystallites, which

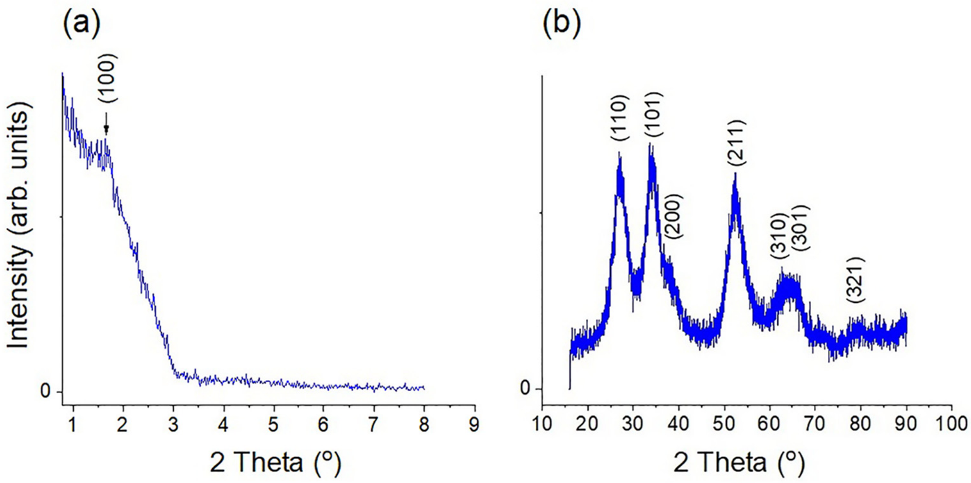

Fig. 1 (a) Small-angle and (b) wide-angle XRD patterns of Sb–SnO_2.

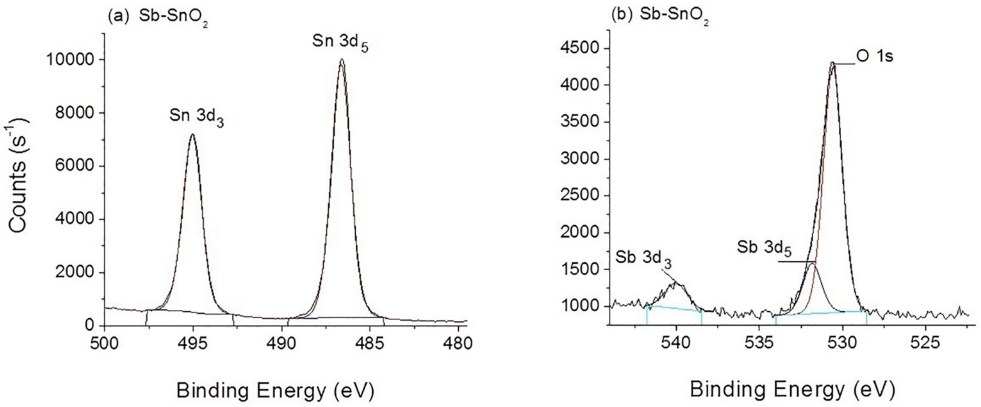

Fig. 2 XPS spectra of Sb–SnO_2. (a) Sn 3d and (b) Sb 3d and O 1S orbitals.

form a continuous framework around the pores. This confirms that the Sb–SnO_2 crystalline structure is chemically connected. The crystallite sizes are approximately 3–4 nm, which is in good agreement with the results obtained from XRD in Section 3.1. We believe that such small crystallite sizes are the result of the short calcination time owing to the extraction of most templating materials before heat treatment. Moreover, no aggregates of Sb_xO_y species were observed in any of the TEM images, confirming that Sb was well incorporated into the framework.

3.5. EDX elemental analysis

The EDX spectrum shows the K and L edges of the elements in the Sb-SnO_2 sample (Fig. 4 (c)), confirming the presence of Sn, O, and Sb atoms. This also signifies that Sb has been successfully incorporated into the Sb-SnO_2 structure. The inset in Fig. 4 (c) shows the atomic percentages (At%) of the elements in a selected area of the sample; however, the At% values in different selected areas were inconsistent. This might be because of the thickness of the sample. With a thicker sample, it is more difficult for the X-ray beam to penetrate the sample layers. Therefore, an average At% of Sb in SnO_2 was calculated and converted into wt%. The determined average Sb content of 4 wt% is similar to that calculated from the XPS data in Section 3.2 and to that added during synthesis (6 wt%). The corresponding EDX mapping images (Fig. 4 (d) and Fig S1) show that all elements are homogeneously distributed throughout the sample. These findings also confirm that Sb (green in Fig. 4 (d) and light blue in Fig. S1) is integrated into the SnO_2 framework and does not aggregate on the sample surface.

3.6. Electrical conductance of Sb–SnO_2

The electrical conductance of Sb–SnO_2 was studied as a function of temperature (Fig. 5). The temperature was increased from 50 to 400 °C in steps of 50 °C. The conductance first increased from 50 to 100 °C, which is typical of semiconductor materials. However, the conductance decreased linearly at higher temperatures because the adsorbed molecular oxygen at the surface was converted to ionic oxygen species (O^- and O^{2-}). This led to electron withdrawal from the surface and a decrease in the overall conductance of the material (Nag et al., 2014). In addition, the intensity of "phonons" increases at higher temperatures, resulting in decreased charge mobility

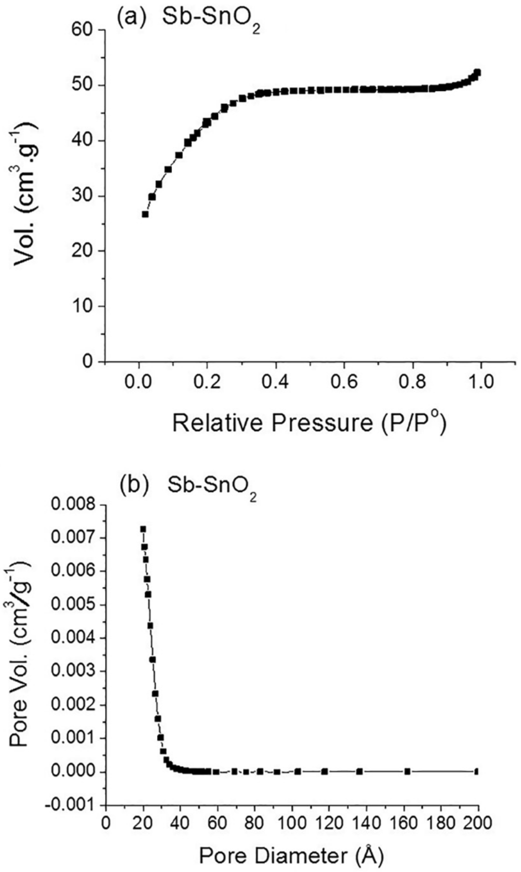

Fig. 3 N_2 sorption analysis of Sb–SnO_2; (a) N_2 isotherm (b) with the corresponding pore size distribution.

and reduced conductance of the material (Terrier et al., 1997). This behavior is typical of semi-metallic materials. Furthermore, the conductance of Sb–SnO_2 at 100 °C (9×10^{-3} S) is approximately one order of magnitude higher than that of pristine SnO_2 (5×10^{-4} S) prepared using the same method (Aqeel et al., 2020). Hence, the significant enhancement in the SnO_2 conductance may result from the presence of electron-donating Sb^{5+} species in the material (Ponja et al., 2018; Yuan et al., 2011). Moreover, we compared the electrical conductance of the Sb–SnO_2 structure with that of pure, doped, and composite SnO_2-based materials (Table 1). These results showed that our Sb–SnO_2 exhibited the highest electrical conductance among others.

3.7. Gas sensing performance of Sb–SnO$_2$-based sensor

To evaluate the gas sensing response of the Sb–SnO_2 structure toward reducing gases, its relative conductance variation (S) was determined using Eq. (1):

$$S = \frac{(G_f - G_0)}{G_0} = \frac{\Delta G}{G_0} \quad (1)$$

Here, G_0 is the conductance of the sensor in the air, and G_f is the conductance in the presence of the analyzed gas.

The response of Sb–SnO_2 toward oxidizing gases was calculated using Eq. (2):

$$S = \frac{(R_f - R_0)}{R_0} = \frac{\Delta R}{R_0} \quad (2)$$

where R_0 is the resistance of the sensing material in the air, and R_f is the resistance in presence of the analyzed gas.

Fig. 6 shows the response of Sb–SnO_2 toward 8 ppm of NO_2, 100 ppm of H_2, and 10 ppm of acetone and ethanol at different temperatures and a relative humidity (RH) of 40%. The Sb–SnO_2-based sensor showed a good response toward NO_2 at 100 °C (Fig. 6 (a)), but was insensitive to the other gases tested (acetone, ethanol, and H_2). At 100 °C, the adsorption of NO_2 on the (1 0 1) (Jiang et al., 2012) and (1 1 0) (Kwon et al., 2016) planes of Sb–SnO_2 is favored. This temperature represents the activation energy required for NO_2 to react with the surface of Sb–SnO_2 (Ngoc et al., 2018), owing to suitable adsorption surface energy and charge transfer. Because NO_2 has a higher electron affinity than the oxygen species (O_2 and O_2^-) on the surface of Sb–SnO_2 at this temperature, interactions between NO_2 and molecular oxygen species result in electron withdrawal (Scheme 2) and thus improved sensing response (Wang et al., 2014). At 200 °C, the sensor response toward NO_2 is further enhanced by approximately three times (Fig. 6 (b)). Herein, in addition to the presence of molecular oxygen (O_2^-), dissociative oxygen (O^-) species start to dominate on the Sb–SnO_2 surface (as an adsorbate), resulting in an improved NO_2 response (Park and Mackenzie, 1996; Yamazoe et al., 2003). However, the response of the sensor to NO_2 decreases at 300 °C, but remains high enough for NO_2 sensing applications (Fig. 6 (c); Table S1). Furthermore, the sensor shows a very weak response to NO_2 at 400 °C, which could be attributed to the higher desorption rate of NO_2 rather than the adsorption rate (Ngoc et al., 2018).

In addition, the Sb–SnO_2-based sensor shows a weak response to H_2 at 300 °C (Fig. 6 (c)), which is the activation energy required for H_2 to interact with the Sb–SnO_2 surface (Sergiienko et al., 2013; Yamazoe et al., 2003; Yang et al., 2010). Furthermore, the response is remarkably enhanced when the temperature of the sensor is increased to 400 °C (Fig. 6 (d)). This is due to the presence of more dissociative oxygen (O^-) species (Park and Mackenzie, 1996; Yamazoe et al., 2003) on the Sb–SnO_2 surface at 400 °C than at 300 °C (Scheme 2). These O^- species interact with H_2, producing water molecules and free electrons (Kwon et al., 2016).

$$H_2 + O^- \rightarrow H_2O + e^-$$

As shown in Fig. 6 (b), the sensor shows a low response toward acetone and ethanol at 200 °C, which corresponds to their activation energy, as confirmed by previous studies (Chen and Cao, 2020; Ngoc et al., 2018); however, it improves significantly at 300 and 400 °C (Fig. 6 (c) and (d)). At 200 °C, ethanol undergoes dehydration and reacts with the adsorbed molecular oxygen species, resulting in a low response (Yamazoe et al., 2003; Lei et al., 2021).

$$CH_3CH_2OH + 3O_2^- \rightarrow 2CO_2 + 3H_2O + 3e^-$$

However, at 300 °C, ethanol undergoes dehydrogenation and reacts with dissociative oxygen species, leading to a higher response.

$$CH_3CH_2OH + O^- \rightarrow CH_3COH + H_2O + e^-$$

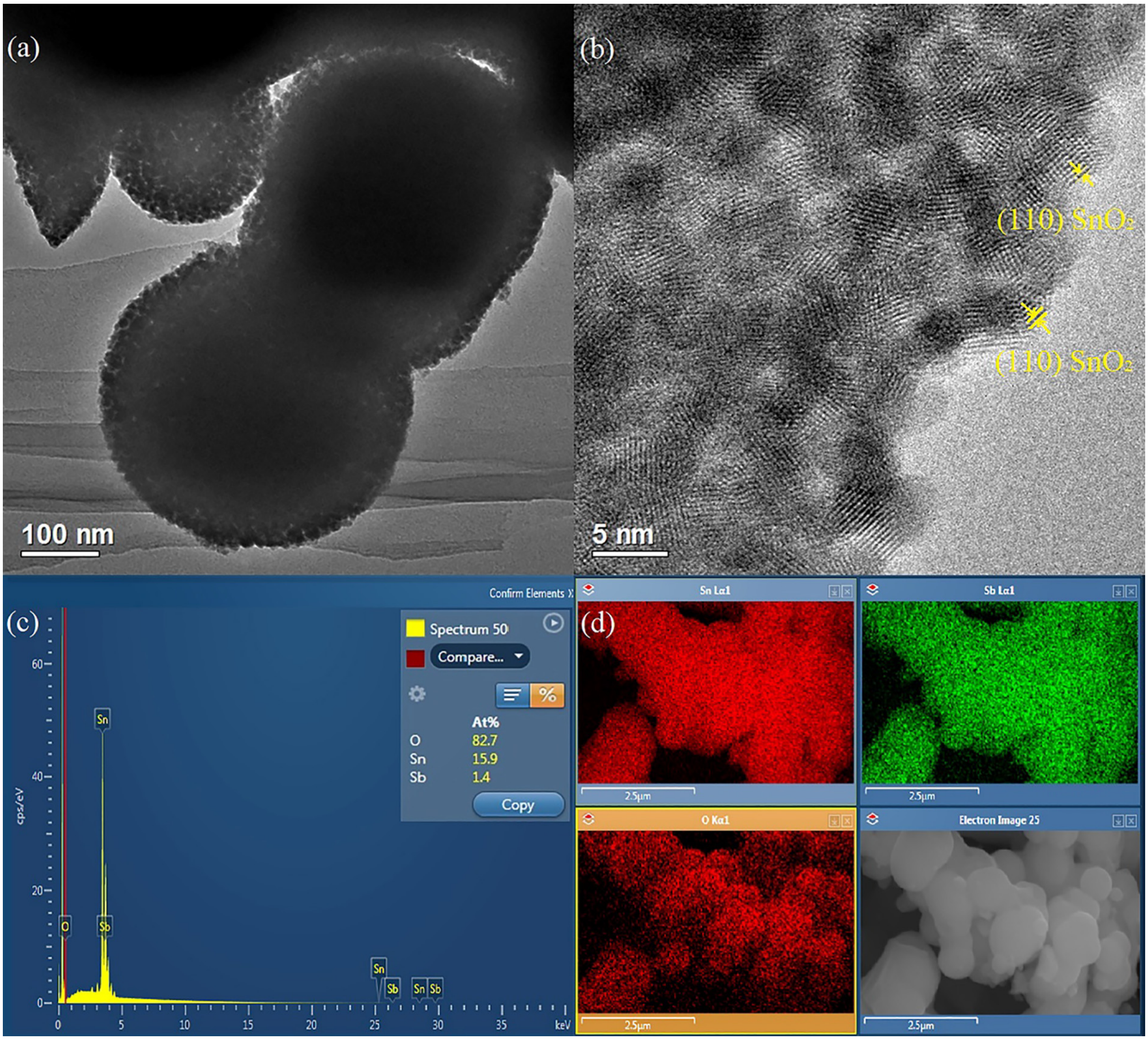

Fig. 4 (a) and (b) TEM images, (c) EDX elemental analysis, and (d) color mapping of Sb–SnO_2. In the mapping, top left: Sn, top right: Sb, and bottom left: O.

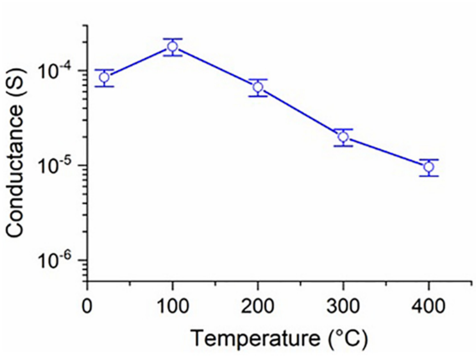

Fig. 5 Temperature-dependent conductance of Sb–SnO_2.

At 400 °C, as the amount of O^- (Eberheim et al., 2003; Yamazoe et al., 2003) on the Sb–SnO_2 surface increases, the response of the material increases accordingly. This enhances ethanol dehydrogenation on basic surfaces and dehydration on acid sites (Eberheim et al., 2003; Yamazoe et al., 2003).

Acetone ($CH_3(C=O)CH_3$) has a carbonyl group ($C=O$) with a partial positive charge on the carbon and a partial negative charge on the oxygen ($C^{\delta+}=O^{\delta-}$), owing to the higher electronegativity of the oxygen. Therefore, the partially positive carbon in acetone is more susceptible to a nucleophilic attack by negatively charged oxygen (O^-) adsorbed on the surface of Sb–SnO_2. Moreover, because Sb is slightly more electronegative than Sn, the oxygen bonded to Sb is more electrophilic and readily attracts the negative double bonds in the acetone molecules (Eberheim et al., 2003).

$$CH_3(C=O)CH_3 + O^- \rightarrow CH_3(C=O)C^+H_2 + H_2O + e^-$$

Table 1 A comparison between the electrical conductance of the pure, doped, and composite SnO_2-based nanomaterials and the Sb–SnO_2 prepared in the present work.

Material	Conductance (S)	Temp. (°C)	References
SnO_2 nanofibers	$1.7 \times 10^{-8} – 2.0 \times 10^{-7}$ $5.0 \times 10^{-8} –5.3 \times 10^{-7}$	100 – 205	Cui, et al., 2022
Pt–SnO_2 nanofibers			
SnO_2	1.1×10^{-5}	275	Sun et al., 2021
SnO_2/Co_3O_4 composites	1.6×10^{-5}		
SnO_2	$3.3 \times 10^{-8} –1.1 \times 10^{-7}$	20 –160	Zhou et al., 2022
Co–SnO_2 nanoparticles	$5.0 \times 10^{-8} –1.0 \times 10^{-5}$		
SnO_2 nanowires	1.0×10^{-7}	300	Kim et al., 2020
SnO_2/Co_3O_4 nanowires/nanoparticles	2.0×10^{-9}		
Spherical mesoporous SnO_2	$1.0 \times 10^{-8}–1.1 \times 10^{-8}$	250	Feng et al., 2021
SnO_2 hollo nanosphere.	1.0×10^{-7}	200	Cai et al., 2021
Pd–SnO_2 hollo–nanosphere	5.0×10^{-8}		
SnO_2	$4.8 \times 10^{-7}– 6.7 \times 10^{-6}$	100 – 450	Nag et al., 2014
Sb–SnO_2	$1.4 \times 10^{-6} – 4.5 \times 10^{-5}$		
Pd–Sb–SnO_2 nanoparticles	$2.5 \times 10^{-7} –1.0 \times 10^{-5}$		
Sb–SnO_2 thin film	9.2×10^{-9}	30 – 80	Panday et al., 2022
SnO_2	5×10^{-4}	100	Aqeel et al., 2020
Sb–SnO_2	9×10^{-3}	100	This work

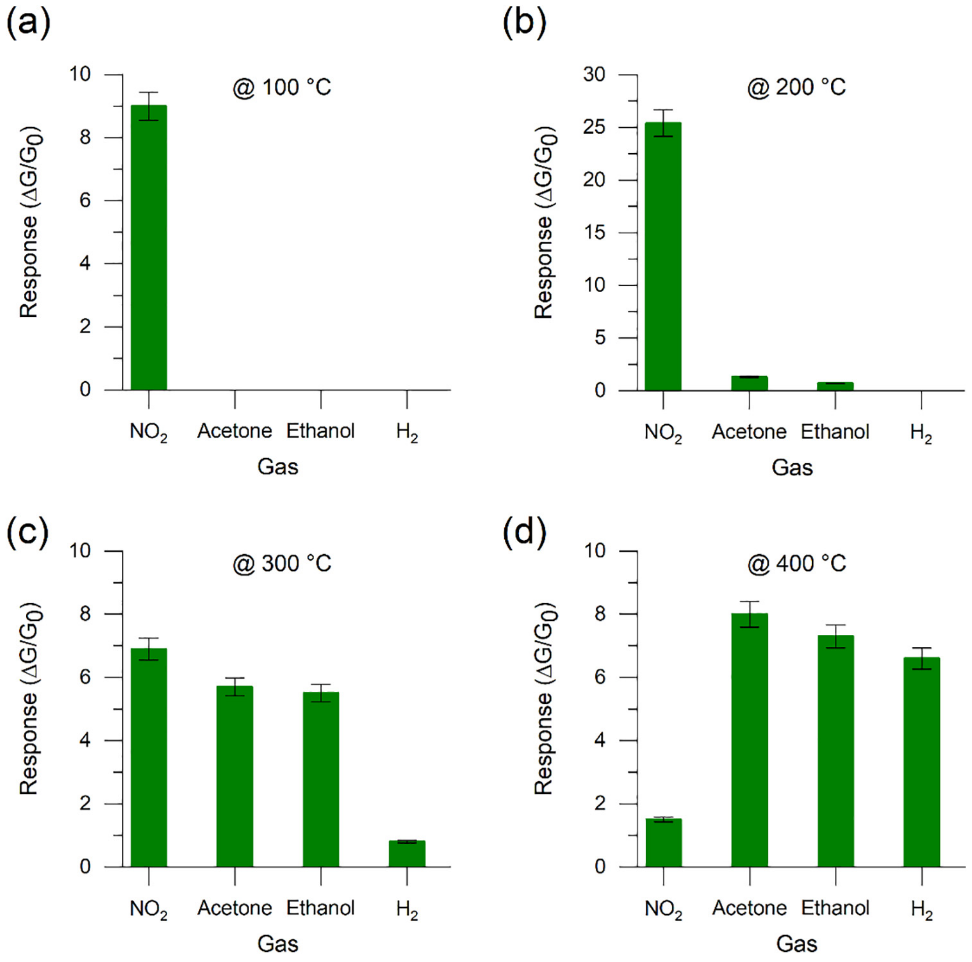

Fig. 6 Responses of the Sb–SnO_2-based sensor toward 8 ppm of NO_2, 10 ppm of acetone, 10 ppm of ethanol, and 100 ppm of H_2 at (a) 100, (b) 200, (c) 300, and (d) 400 °C. Relative humidity (RH) in the test chamber was set to 40%.

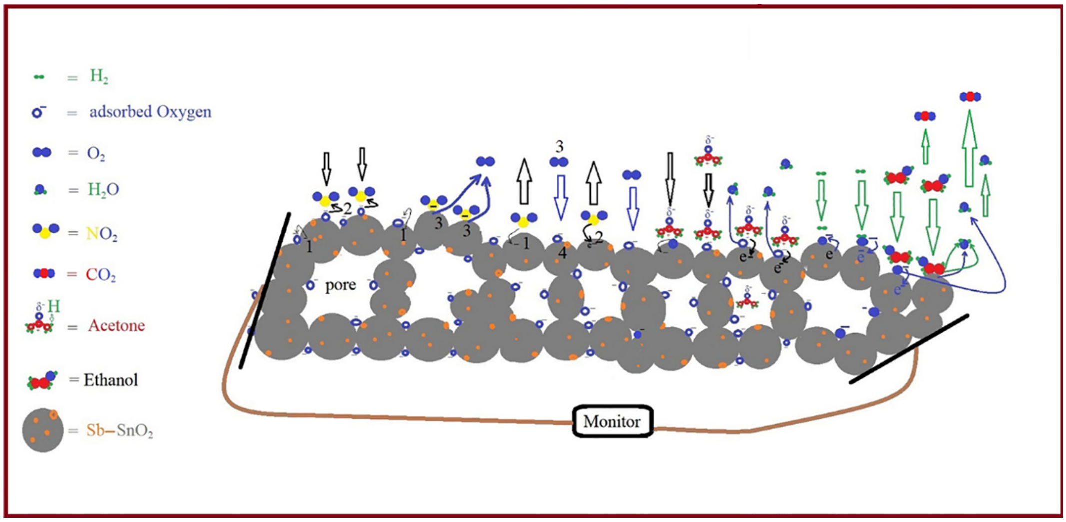

Scheme 2 Schematic illustration of gas sensing mechanisms.

Table 2 Comparison between the gas-sensing properties of the Sb–SnO_2 material and other recently reported metal oxide nanomaterials and nanocomposites toward acetone and NO_2.

Materials	Analyte	Concentration (ppm)	Response	Sensing temperature (°C)	References
ZnO nano–cactus	Acetone	10–500	1–3.4	230	Islam et al. 2021
Mesoporous ZnO	Acetone	50	1.8	200	Lei et al., 2021
Mesoporous ZnO–Au	Acetone	50	37	200	
SnO_2 hollow nanosphere	Acetone	1–100	1–6	200	Cai et al., 2021
Pd–SnO_2 hollow nanosphere	Acetone	1–100	1–15	200	
$BiFeO_3$	Acetone	1–50	2.5–18.5	244	Xu et al., 2022
Sr–$BiFeO_3$ nanomaterial	Acetone	1–50	2.5 –24.7	208	
Co_3O_4	Acetone	50	3	240	Fan et al., 2023
Co_3O_4 halloysites nanotubes	Acetone	50	7	240	
SnO_2	Acetone	50	4	170	Zhang et al., 2022
Ag–SnO_2 nanosheets	Acetone	50	5	170	
SnO_2	Acetone	100	10	110	Jawaher et al., 2018
CeO_2	Acetone	100	5	110	
CeO_2–SnO_2 nanocomposites	Acetone	100	16	110	
MoO_3 nanorods	Acetone	10	1.2	200	Meng et al., 2022
$NiMoO_4$/MoO_3 composites	Acetone	10	1.9	200	
SnO_2	Acetone	10	2	160	Han et al., 2022
PtCu–SnO_2 nanoparticles	Acetone	10	2.5	160	
Porous $ZnSnO_3$ nanocubes	Acetone	50	4.7	210	Zheng et al., 2021
Porous SnO_2 nanoparticles	Acetone	1	0.2	150	John et al., 2021
	NO_2	1	1.3	150	
ZnO/SnO_2 nanoparticles	Acetone	–	–	150	
	NO_2	1	0.9	150	
3-nm ZIF-8/SnO_2 nanoparticles	Acetone	1	0.1	150	
	NO_2	1	0.6	150	
$BiFeO_3$ hollow microcubes	Acetone	200	5.2	240	Yu et al., 2021
SnO_2	Acetone	5	3.47	400	Koo et al., 2017
PdO@ZnO/SnO_2 nanofibers	Acetone	5	6.55	400	
SnO_2	Acetone	5	5.45	400	
PdO@ZnO/SnO_2 nanotubes	Acetone	5	10.12	400	
SnS	Acetone	25	1.12	RT	Bai et al., 2021
Mn/SnS nanoflakes	Acetone	25	3.7	RT	
Spherical mesoporous SnO_2	Acetone	50	1.2	250	Feng et al., 2021
	NO_2	50	2.2		
Mesoporous Sb–SnO_2	Acetone	1.5–10	4–8	400	This work
	Acetone	1.5–10	3.6–5.7	300	
	NO_2	8	25	200	
	NO_2	1–8	2.5–6.9	300	

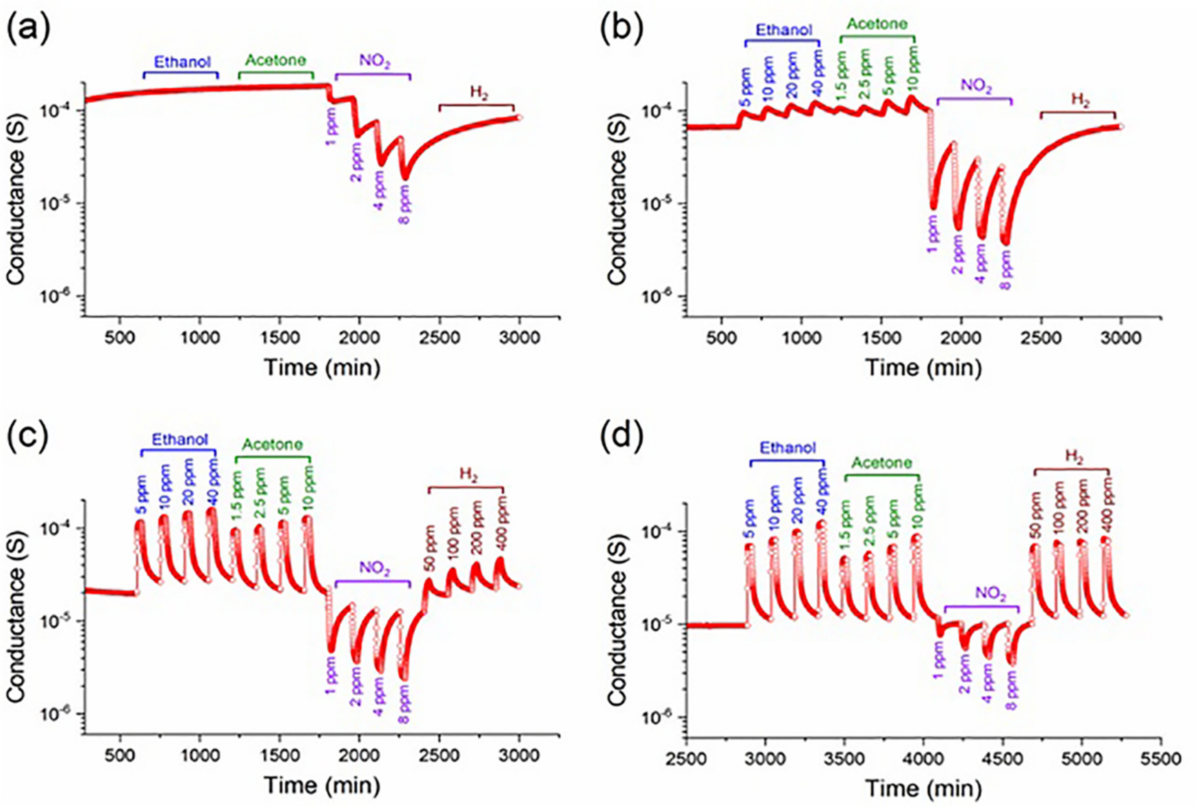

Fig. 7 Dynamic responses of the Sb–SnO$_2$-based sensor at different concentrations of ethanol, acetone, NO$_2$, and H$_2$ at (a) 100, (b) 200, (c) 300, and (d) 400 °C.

As a result, the sensor responded more strongly to acetone than to ethanol at 300 and 400 °C (Fig. 6 (c) and (d)). Thus, the oxidation of ethanol and acetone is more effective at higher operating temperatures (Chakraborty et al., 2021; Eberheim et al., 2003). The schematic of the interactions between gaseous compounds and the surface of Sb–SnO$_2$ is presented in Scheme 2.

The porous structure of Sb–SnO$_2$ with a relatively large surface area (155 m^2 g^{-1}) facilitates enhanced diffusion of gases/vapors and promotes interactions between gases and adsorbed oxygen species on the sensor surface (Koo et al., 2017). Moreover, despite the simple synthesis procedure of Sb–SnO$_2$, the responses of our sensor to various gas concentrations are comparable with those of previously reported more complicated material structures (Kim et al., 2021; Koo et al., 2017; Vishwakarma and Yadava, 2021). Furthermore, the synthesized Sb–SnO$_2$ exhibits superior sensing performance toward acetone and NO$_2$ compared to the spherical porous SnO$_2$ nanostructure (Feng et al., 2021). Table 2 shows a comparison between the sensing response of the Sb–SnO$_2$ structure and other pure and composite materials toward acetone and NO$_2$. Evidently, Sb–SnO$_2$ demonstrated an excellent sensing response to low concentrations of acetone and NO$_2$ compared to recently reported gas sensors based on other metal oxide nanocomposites.

The dynamic responses of the Sb–SnO$_2$-based sensor at different gas concentrations and temperatures are shown in Fig. 7. As shown in Fig. 7 (a) and (b), the baseline for NO$_2$ is not recovered after the gas was turned off at 100 and 200 °C. This may be because NO$_2$, being a strong oxidizing gas, strongly holds the adsorbed electrons, making it difficult for the synthetic air to release these electrons and exchange them with the oxygen molecules present in the test chamber at these temperatures (Li et al., 2015). At 300 and 400 °C, our sensor shows reversible dynamic responses toward all tested gases (Fig. 7 (c) and (d)). Moreover, the dynamic responses are proportional to the gas concentrations, which is crucial for their quantitative analysis. Furthermore, our Sb–SnO$_2$-based sensor exhibits an excellent response to low concentrations of acetone (1.5 ppm) and NO$_2$ (1 ppm) (Fig. 7 (c) and (d)). These results could be attributed to the small crystallite size and large surface area of the fabricated porous Sb–SnO$_2$ nanostructures (Yamazoe et al., 2003). However, while the response towards NO$_2$ decreases significantly, the response to H$_2$ increases significantly at 400 °C (Tables S1 and S2). It is worth noting that the sensing behavior of Sb–SnO$_2$ is typical of an *n*-type material. Therefore, the conductance of the Sb–SnO$_2$-based sensor increases upon exposure to reducing gases, such as H$_2$, ethanol, and acetone, whereas it decreases when exposed to an oxidizing gas, such as NO$_2$. One possible explanation for the decreased conductance is that NO$_2$ is more electronegative than molecular oxygen and thus withdraws electrons from the Sb–SnO$_2$ conduction band, resulting in a lower concentration of surface electrons and overall conductance of Sb–SnO$_2$.

4. Conclusion

We successfully synthesized crystalline mesoporous Sb–SnO$_2$ nanostructures at ambient pressure and temperature using our modified method. According to the XRD and TEM analyses, the Sb–SnO$_2$ crystallites with a size of 3–4 nm were chemically connected and formed a continuous framework. Furthermore, the Sb–SnO_2 nanostructure exhibited a large BET surface area (155 m^2 g^{-1}) with a narrow pore size distribution (2–3 nm), which is favorable for excellent gas adsorption in a sensor. The small crystallite and pore sizes result from a short calcination time and efficient removal of the templating materials via Soxhlet extraction. In addition, a higher electrical conductance of the Sb–SnO_2 material was achieved compared to the previously reported pristine SnO_2 prepared using the same method, other SnO_2 composites, and oxide materials. Based on the XPS, XRD, and EDS results, the presence of electron-donating Sb^{5+} in the (Sb_2O_5) framework could explain the enhanced conductance of our material. The gas sensing performance of the Sb–SnO_2-based sensor in the presence of reducing and oxidizing gases was highly dependent on the operating temperature. Thus, the sensor exhibited a very high response to NO_2 between 100 and 300 °C. However, efficient desorption of NO_2 was not achieved at 100 and 200 °C, and the conductance of the sensor did not recover to its baseline value. Conversely, Sb–SnO_2 exhibited a high and reversible response to low concentrations (1 ppm) of NO_2 at 300 °C. studies of the sensing properties of Sb–SnO_2 toward acetone and ethanol showed that the increase in the operating temperature and the high number of dissociative oxygen species improved the interactions between the sensor and the gases, ensuring a high sensing response. In addition, the Sb–SnO_2 sensor exhibited a slightly higher response to low concentrations of acetone compared to ethanol. Furthermore, the formation of O^- species on the surface of Sb–SnO_2 and their increased concentration at higher temperatures played a key role in improving the sensing response toward H_2. Thus, these findings demonstrate that the synthesis method described in this work can be used to fabricate nanocrystalline doped oxide materials with high conductivity and excellent sensing performance. In light of these findings, we will continue to investigate different Sb concentrations and elements that can be introduced into the SnO_2 framework to determine an optimal composition for detecting a specific gaseous compound and studying the effect of humidity on sensor performance.

Author contributions

T.A. synthesized the materials and performed structural and compositional analyses using EDX, XRD, TEM, and N_2 sorption analysis, discussed the TEM, EDX, XRD, and part of the N_2 sorption results in the manuscript, the relation between the structure and the gas interaction. T.A. wrote most of the manuscript and provided partial financial support from PAAET. V.G. prepared samples for the gas sensing characterization. V.G. and E.C. performed the gas sensing tests, discussed the corresponding results, and provided partial financial support for the gas sensing characterizations. Both E.C. and V.G. proofread and revised the manuscript many times during the writing process. A.B. supervised, analyzed, and discussed the results obtained from the XPS test, discussed one part of the N_2 sorption results, and proofread the final version of the manuscript.

Declaration of Competing Interest

The authors declare that they have no known competing financial interests or personal relationships that could have appeared to influence the work reported in this paper.

Acknowledgment

This work was partially funded by the Public Authority of Applied Education and Training (PAAET), Kuwait (Project No. BE-16-05 titled “Synthesis of crystalline mesoporous tin dioxide framework doped with fluoride and antimony to improve its electrical and optical properties”) and carried out in collaboration with Kuwait University. The assistance provided for the XPS measurements at Kuwait University (Project No. GS01/05) is acknowledged. The work was also funded by the “Multi-Messenger and Machine Learning Monitoring of SARS-CoV-2 for Occupational Health & Safety” (4 M SARS-CoV-2) project under the Special Integrative Fund for Research (FISR), Ministry of University and Research (MUR), Italy, NATO Science for Peace and Security Program under Grant No. G5634 “Advanced Electro-Optical Chemical Sensors”, and the “Smart Cities and Communities and Social Innovation” project titled “SWaRM Net/Smart Water Resource Management – Networks” (MUR).

Appendix A. Supplementary material

Supplementary data to this article can be found online at https://doi.org/10.1016/j.arabjc.2023.104797.

References

Aegerter, M.A., Reich, A., Ganz, D., Gasparro, G., Pütz, J., Krajewski, T., 1997. Comparative study of SnO_2: Sb transparent conducting films produced by various coating and heat treatment techniques. J. Non-Cryst. Solids 218, 123–128. https://doi.org/10.1016/S0022-3093(97)00134-8.

Aqeel, T., Greer, H.F., Zhou, W.Z., Bruce, D.W., Bumajdad, A., 2016. Novel direct synthesis of mesoporous tin dioxide network intact up to 500 °C. J. Nano Res. 40, 79–89. https://doi.org/10.4028/www.scientific.net/JNanoR.40.79.

Aqeel, T., Galstyan, V., Comini, E., 2020. Mesoporous polycrystalline SnO_2 framework synthesized by direct soft templating method for highly selective detection of NO_2. Nanotechnology 31,. https://doi.org/10.1088/1361-6528/ab5a1e 105502.

Aswaghosh, L., Manoharan, D., Jaya, N.V., 2016. Defect structure and optical phonon confinement in ultrananocrystalline $Bi_xSn_{1-x}O_2$ (x = 0, 0.03, 0.05, and 0.08) synthesized by a sonochemical method. Phys. Chem. Chem. Phys. 18, 5995–6004. https://doi.org/10.1039/C5CP06214D.

Bai, Y., Qin, Y., Qiu, P., 2021. Boosting the acetone sensing of SnS nanoflakes by spin Mn substitution: a novel adsorption-desorption perspective. Environ. Sci. Nano 8, 1096–1108. https://doi.org/10.1039/D0EN01251C.

Benhebal, H., Chaib, M., Léonard, A., Lambert, S.D., Crine, M., 2011. Synthesis, characterization and photocatalytic properties of alkali metals doped tin dioxide. J. Mol. Struct. 1004, 222–226. https://doi.org/10.1016/j.molstruc.2011.08.009.

Brunet, E., Maier, T., Mutinati, G.C., Steinhauer, S., Köck, A., Gspan, C., Grogger, W., 2012. Comparison of the gas sensing performance of SnO_2 thin film and SnO_2 nanowire sensors. Sensors Actuators, B 165, 110–118. https://doi.org/10.1016/j.snb.2012.02.025.

Brus, L.E., 1984. Electron-electron and electron-hole interactions in small semiconductor crystallites: the size dependence of the lowest excited electronic state. J. Chem. Phys. 80, 4403–4409. https://doi.org/10.1063/1.447218.

Cai, Z., Goo, E., Park, S., 2021. Hydrogen sensing performance and its enhanced sensing mechanisms of hollow structured-SnO_2 nanospheres activated by noble metal nanoparticles. J. Mater. Res. Technol. 15, 1716–1731. https://doi.org/10.1016/j.jmrt.2021.09.022.

Chakraborty, N., Das, S., Srihari, V., Mondal, D.J., Saha, D., Konar, S., Mishra, A.K., Mondal, S., 2021. Roles of structure and electron mobilization in enhanced ethanol sensing by Al doped SnO_2 nanoparticles. Mater. Adv. 2, 3760–3769. https://doi.org/10.1039/D1MA00172H.

Chen, F., Liu, M., 1999. Preparation of mesoporous tin oxide for electrochemical applications. Chem. Commun. 1829–1830. https://doi.org/10.1039/A904142G

Chen, Y., Cao, Y., 2020. Ultrasensitive and low detection limit of acetone gas sensor based on ZnO/SnO_2 thick films. RSC Adv. 10, 35958–35965. https://doi.org/10.1039/D0RA06406H.

Chen, G., Seo, J., Yang, C., Prasad, P.N., 2013. Nanochemistry and nanomaterials for photovoltaics. Chem. Soc. Rev. 42, 8304–8338. https://doi.org/10.1039/C3CS60054H.

Chowdhury, N.K., Bhowmik, B., 2021. Micro/nanostructured gas sensors: the physics behind the nanostructure growth, sensing and selectivity mechanisms. Nanoscale Adv. 3, 73–93. https://doi.org/10.1039/D0NA00552E.

Cui, S., Qin, J., Liu, W., 2022. Ultrafine Pt-doped SnO_2 mesopore nanofibers-based gas sensor for enhanced acetone sensing. Chin. J. Anal. Chem. 100188. https://doi.org/10.1016/j.cjac.2022.100188.

Das, A., Bonu, V., Prasad, A.K., Panda, D., Tyagi, A.K., 2014. The role of SnO_2 quantum dots in improved CH_4 sensing at low temperature. J. Mater. Chem. C 2, 164–171. https://doi.org/10.1039/C3TC31728E.

Das, R., Vecitis, C.D., Schulze, A., Cao, B., Ismail, A.F., Lu, X., Chen, J., Ramakrishna, S., 2017. Recent advances in nanomaterials for water protection and monitoring. Chem. Soc. Rev. 46, 6946–7020. https://doi.org/10.1039/C6CS00921B.

Du, Y., Yan, J., Meng, Q., Wang, J., Dai, H., 2012. Fabrication and excellent conductive performance of antimony-doped tin oxide-coated diatomite with porous structure. Mater. Chem. Phys. 133, 907–912. https://doi.org/10.1016/j.matchemphys.2012.01.115.

Eberheim, A., Kohl, D., Schierberle, P., 2003. Tin oxide sensor element for the detection of organic compounds with hydroxy groups. Phys. Chem. Chem. Phys. 5, 5203–5206. https://doi.org/10.1039/B307501J.

Fan, J., Yang, C., Zhao, X., Li, D., Xiao, F., Wu, R., Wang, L., 2023. Enhanced gas sensing property of Co_3O_4 matrix nanocomposites with halloysite nanotubes toward triethylamine. J. Mater. Res. Technol. 23, 2491–2503. https://doi.org/10.1016/j.jmrt.2023.01.142.

Feng, B., Feng, Y., Qin, J., Wang, Z., Zhang, Y., Du, F., Zhao, Y., Wei, J., 2021. Self-template synthesis of spherical mesoporous tin dioxide from tin-polyphenol-formaldehyde polymers for conductometric ethanol gas sensing. Sensors Actuators, B 341,. https://doi.org/10.1016/j.snb.2021.129965 129965.

Feng, B., Wu, Y., Ren, Y., Chen, Y., Yuan, K., Deng, Y., Wei, J., 2022. Self-template synthesis of mesoporous Au-SnO_2 nanospheres for low-temperature detection of triethylamine vapor. Sensors Actuators, B 356,. https://doi.org/10.1016/j.snb.2021.131358 131358.

Ganose, A.M., Scanlon, D.O., 2016. Band gap and work function tailoring of SnO_2 for improved transparent conducting ability in photovoltaics. J. Mater. Chem. C 4, 1467–1475. https://doi.org/10.1039/C5TC04089B.

Goebbert, C., Aegerter, M.A., Burgard, D., Nassb, R., Schmidt, H., 1999. Ultrafiltration conducting membranes and coatings from. J. Mater. Chem. 9, 253–258. https://doi.org/10.1039/A805082A.

Han, Z., Tang, Y., Lu, G., Qi, Y., Wu, H., Yang, Z., Han, H., Zhang, X., Wu, L., Wang, Z., Liu, J., Wang, F., 2022. PtCu-SnO_2 nanocomposites for ultrasensitive and rapid ultra-low formaldehyde sensing. ChemPhysMater 1, 227–236. https://doi.org/10.1016/j.chphma.2022.03.007.

Hao, T., Cheng, G., Ke, H., Zhu, Y., Fu, Y., 2014. Effects of fluorine ions on the formation and photocatalytic activities of SnO_2 nanoparticles with small sizes. RSC Adv. 4, 21548–21552. https://doi.org/10.1039/C4RA02802C.

Hou, K., Puzzo, D., Helander, M.C., Lo, S.S., Bonifacio, L.D., Wang, W., Lu, Z.H., Scholes, G.D., Ozin, G.A., 2009. Dye-anchored mesoporous antimony-doped tin oxide electrochemiluminescence cell. Adv. Mater. 21, 2492–2496. https://doi.org/10.1002/adma.200803330.

Huang, B.J., Li, F., Zhang, C.W., Li, P., Wang, P.J., 2014. Electronic structure and optical properties of Ag-doped SnO_2 nanoribbons. RSC Adv. 4, 41819–41824. https://doi.org/10.1039/C4RA05428H.

Islam, M., Srivastava, A.K., Basavaraja, B.M., Sharma, A., 2021. "Nano-on-Micro" approach enables synthesis of ZnO nano-cactus for gas sensing applications. Sens. Int. 2,. https://doi.org/10.1016/j.sintl.2021.100084 100084.

Jawaher, K.R., Indirajith, R., Krishnan, S., Robert, R., Pasha, S.K.K., Deshmukh, K., Das, S.J., 2018. Hydrothermal synthesis of CeO_2–SnO_2 nanocomposites with highly enhanced gas sensing performance towards n-butanol. J. Sci.: Adv. Mater. Devices 3, 139–144. https://doi.org/10.1016/j.jsamd.2018.03.006.

Jiang, C., Zhang, G., Wu, Y., Li, L., Shi, K., 2012. Facile synthesis of SnO_2 nanocrystalline tubes by electrospinning and their fast response and high sensitivity to NOx at room temperature. CrystEngComm 14, 2739–2747. https://doi.org/10.1039/C2CE06405G.

John, A.T., Murugappan, K., Taheri, M., Nisbet, D.R., Tricoli, A., 2021. Tuning the selectivity of highly sensitive chemiresistive nanoparticle networks by encapsulation with metal-organic frameworks. J. Mater. Chem. C 9, 17331–17340. https://doi.org/10.1039/D1TC03606H.

Kim, H., Cai, Z., Chang, S.P., Park, S., 2020. Improved sub-ppm acetone sensing properties of SnO_2 nanowire-based sensor by attachment of Co_3O_4 nanoparticles. J. Mater. Res. Technol. 9, 1129–1136. https://doi.org/10.1016/j.jmrt.2019.12.094.

Kim, S., Singh, G., Oh, M., Lee, K., 2021. An analysis of a highly sensitive and selective hydrogen gas sensor based on a 3D Cu-doped SnO_2 sensing material by efficient electronic sensor interface. ACS Sens. 6, 4145–4155. https://doi.org/10.1021/acssensors.1c01696.

Kojima, M., Kato, H., Gatto, M., 1997. Microstructure and electrical properties of Sb-Sn-O thin films. J. Non-Cryst. Solids 218, 230–234. https://doi.org/10.1016/S0022-3093(97)00142-7.

Koo, W.T., Jang, J.S., Choi, S.J., Cho, H.J., Kim, I.D., 2017. Metal–organic framework templated catalysts: dual sensitization of PdO–ZnO composite on hollow SnO_2 nanotubes for selective acetone sensors. ACS Appl. Mater. Interfaces 9, 18069–18077. https://doi.org/10.1021/acsami.7b04657.

Kwon, Y.J., Kang, S.Y., Wu, P., Peng, Y., Kim, S.S., Kim, H.W., 2016. Selective improvement of NO_2 gas sensing behavior in SnO_2 nanowires by ion-beam irradiation. ACS Appl. Mater. Interfaces 8, 13646–13658. https://doi.org/10.1021/acsami.6b01619.

Lei, M., Gao, M., Yang, X., Zou, Y., Alghamdi, A., Ren, Y., Deng, Y., 2021. Size-controlled Au nanoparticles incorporating mesoporous ZnO for sensitive ethanol sensing. ACS Appl. Mater. Interfaces 13, 51933–51944. https://doi.org/10.1021/acsami.1c07322.

Li, X., Cho, J.H., Kurup, P., Gu, Z., 2012. Novel sensor array based on doped tin oxide nanowires for organic vapor detection. Sens. Actuators, B 162, 251–258. https://doi.org/10.1016/j.snb.2011.12.075.

Li, L., Zhang, C., Chen, W., 2015. Fabrication of SnO_2-SnO nanocomposites with p-n heterojunctions for the low-temperature sensing of NO_2 gas. Nanoscale 7, 12133–12142. https://doi.org/10.1039/C5NR02334C.

Liu, S., Ding, W., Gu, Y., Chai, W., 2012. Effect of Sb doping on the microstructure and optoelectrical properties of Sb-doped SnO_2 films prepared by spin coating. Phys. Scr. 85,. https://doi.org/10.1088/0031-8949/85/06/065601 065601.

Manikandan, M., Tanabe, T., Ramesh, G. V., Kodiyath, R., Ueda, S., Sakuma, Y., Homma, Y., Dakshanamoorthy, A., Ariga, K., Abe, H., 2016. Tailoring the surface-oxygen defects of a tin dioxide support towards an enhanced electrocatalytic performance of platinum nanoparticles. Phys. Chem. Chem. Phys. 18, 5932–5937. https://doi.org/10.1039/C5CP04714E.

Martinez, C.J., Hockey, B., Montgomery, C.B., Semancik, S., 2005. Porous tin oxide nanostructured microspheres for sensor applications. Langmuir 21, 7937–7944. https://doi.org/10.1021/la050118z.

Masuda, Y., 2022. Recent advances in SnO_2 nanostructure based gas sensors. Sens. Actuators, B 364,. https://doi.org/10.1016/j.snb.2022.131876 131876.

Meng, D., Li, R., Zhang, L., Wang, G., Zhang, Y., San, X., Wang, X., 2022. Synthesis of $NiMoO_4$-functionalized MoO_3 nanorods with enhanced TMA gas sensing properties. Sens. Actuators Rep. 4, 100104.

Morris, L., Williams, D.E., Kaltsoyannis, N., Tocher, D.A., 2001. Surface grafting as a route to modifying the gas-sensitive resistor properties of semiconducting oxides: Studies of Ru-grafted SnO_2. Phys. Chem. Chem. Phys. 3, 132–145. https://doi.org/10.1039/B006551J.

Müller, V., Rasp, M., Stefanic, G., Günther, S., Rathousky, J., Niederberger, M., Fattakhova-Rohlfing, D., 2011. Antimony doped tin oxide nanoparticles and their assembly in mesostructured film. Phys. Status Solidi C Top. Solid State Phys. 8, 1759–1763. https://doi.org/10.1002/pssc.201000129.

Nag, P., Majumdar, S., Bumajdad, A., Devi, P.S., 2014. Enhanced gas sensing performance of tin dioxide-based nanoparticles for a wide range of concentrations of hydrogen gas. RSC Adv. 4, 18512–18521. https://doi.org/10.1039/C3RA48060G.

Ngoc, T.M., Van Duy, N., Hung, C.M., Hoa, N.D., Trung, N.N., Nguyen, H., Van Hieu, N., 2018. Ultralow power consumption gas sensor based on a self-heated nanojunction of SnO_2 nanowires. RSC Adv. 8, 36323–36330. https://doi.org/10.1039/C8RA06061D.

Noor, N., Parkin, I.P., 2013. Enhanced transparent-conducting fluorine-doped tin oxide films formed by Aerosol-assisted chemical vapour deposition. J. Mater. Chem. C 1, 984–996. https://doi.org/10.1039/C2TC00400C.

Noor, N., Chew, C.K.T., Bhachu, D.S., Waugh, M.R., Carmalt, C.J., Parkin, I.P., 2015. Influencing FTO thin film growth with thin seeding layers: a route to microstructural modification. J. Mater. Chem. C 3, 9359–9368. https://doi.org/10.1039/C5TC02144H.

Oakton, E., Tillier, J., Siddiqi, G., Mickovic, Z., Sereda, O., Fedorov, A., Copéret, C., 2016. Structural differences between Sb- and Nb-doped tin oxides and consequences for electrical conductivity. New J. Chem. 40, 2655–2660. https://doi.org/10.1039/C5NJ03182F.

Oh, H.S., Nong, H.N., Strasser, P., 2015. Preparation of mesoporous Sb-, F-, and in-doped SnO_2 bulk powder with high surface area for use as catalyst supports in electrolytic cells. Adv. Funct. Mater. 25, 1074–1081. https://doi.org/10.1002/adfm.201401919.

Panday, M., Upadhyay, G., Purohit, L., 2022. Sb incorporated SnO_2 nanostructured thin films for CO_2 gas sensing and humidity sensing applications. Journal of Alloys and Compounds 904, 164053. https://doi.org/10.1016/j.jallcom.2022.164053.

Park, S.S., Mackenzie, J.D., 1996. Thickness and microstructure effects on alcohol sensing of tin oxide thin films. Thin Solid Films 274, 154–159. https://doi.org/10.1016/0040-6090(95)07075-3.

Ponja, S.D., Williamson, B.A.D., Sathasivam, S., Scanlon, D.O., Parkin, I.P., Carmalt, C.J., 2018. Enhanced electrical properties of antimony doped tin oxide thin films deposited via aerosol assisted chemical vapour deposition. J. Mater. Chem. C 6, 7257–7266. https://doi.org/10.1039/C8TC01929K.

Popescu, D.A., Herrmann, J.M., Chimie, Ensuque, A., Bozon-Verduraz, F., 2001. Nanosized tin dioxide : Spectroscopic (UV–VIS , NIR , EPR) and electrical conductivity studies. Phys. Chem. Chem. Phys. 3, 2522–2530. https://doi.org/10.1039/B100553G

Sergiienko, S.A., Kukla, O.L., Yaremov, P.S., Solomakha, V.N., Shvets, O.V., 2013. The influence of preparation conditions and doping on the physicochemical and sensor properties of mesoporous tin oxide. Sens. Actuators, B 177, 643–653. https://doi.org/10.1016/j.snb.2012.11.008.

Severin, K.G., Abdel-Fattah, T.M., 1998. Supramolecular assembly of mesostructured tin oxide. Chem. Commun. 1471–1472. https://doi.org/10.1039/A709067F

Shaalan, N.M., Hamad, D., Abdel-Latief, A.Y., Abdel-Rahim, M.A., 2016. Preparation of quantum size of tin oxide: structural and physical characterization. Prog. Nat. Sci. Mater. Int. 26, 145–151. https://doi.org/10.1016/j.pnsc.2016.03.002.

Shao, S., Koehn, R., Wu, H., Wu, T., Rao, W.F., 2016. Generation of highly ordered nanoporous Sb–SnO_2 thin films with enhanced ethanol sensing performance at low temperature. New J. Chem. 40, 5523–5530. https://doi.org/10.1039/C5NJ03463A.

Shokr, E.K., Wakkad, M.M., Abd El-Ghanny, H.A., Ali, H.M., 2000. Sb-doping effects on optical and electrical parameters of SnO_2 films. J. Phys. Chem. Solids 61, 75–85. https://doi.org/10.1016/S0022-3697(99)00234-6.

Smith, A.M., Nie, S., 2011. Bright and compact alloyed quantum dots with broadly tunable near-infrared absorption and fluorescence spectra through mercury cation exchange. J. Am. Chem. Soc. 133, 24–26. https://doi.org/10.1021/ja108482a.

Suh, J.M., Eom, T.H., Cho, S.H., Kim, T., Jang, H.W., 2021. Light-activated gas sensing: A perspective of integration with micro-LEDs and plasmonic nanoparticles. Mater. Adv. 2, 827–844. https://doi.org/10.1039/D0MA00685H.

Sun, L., Yuan, X., Sun, J., Zhang, K., Liao, D., Chen, S., 2021. Bimetallic organic framework-derived SnO_2/Co_3O_4 heterojunctions for highly sensitive acetone sensors. New J. Chem. 45, 18150–18157. https://doi.org/10.1039/D1NJ03025F.

Terrier, C., Chatelon, J.P., Roger, J.A., 1997. Electrical and optical properties of Sb:SnO_2 thin films obtained by the sol-gel method. Thin Solid Films 295, 95–100. https://doi.org/10.1016/S0040-6090(96)09324-8.

Thommes, M., Kaneko, K., Neimark, A.V., Olivier, J.P., Rodriguez-Reinoso, F., Rouquerol, J., Sing, K.S.W., 2015. Physisorption of gases, with special reference to the evaluation of surface area and pore size distribution (IUPAC Technical Report). Pure Appl. Chem. 87, 1051–1069. https://doi.org/10.1515/pac-2014-1117.

Vishwakarma, A.K., Yadava, L., 2021. Structural and sensing properties of ethanol gas using Pd-doped SnO_2 thick film gas sensor. Environ. Sci. Pollut. Res. 28, 3920–3927. https://doi.org/10.1007/s11356-020-10211-6.

Wagner, T., Bauer, M., Sauerwald, T., Kohl, C.D., Tiemann, M., 2011. X-ray absorption near-edge spectroscopy investigation of the oxidation state of Pd species in nanoporous SnO_2 gas sensors for methane detection. Thin Solid Films 520, 909–912. https://doi.org/10.1016/j.tsf.2011.04.187.

Wang, Y., Brezesinski, T., Antonietti, M., Smarsly, B., 2009. Ordered Mesoporous Sb-, Nb-, and Ta-doped SnO2 thin films with adjustable doping levels and high electrical conductivity. ACS Nano 3, 1373–1378. https://doi.org/10.1021/nn900108x.

Wang, X., Qiu, S., Liu, J., He, C., Lu, G., Liu, W., 2014. Synthesis of mesoporous SnO_2 spheres and application in gas sensors. Eur. J. Inorg. Chem. 863–869. https://doi.org/10.1002/ejic.201301212

Wang, G., Yang, S., Cao, L., Jin, P., Zeng, X., Zhang, X., Wei, J., 2021. Engineering mesoporous semiconducting metal oxides from metal-organic frameworks for gas sensing. Coord. Chem. Rev. 445,. https://doi.org/10.1016/j.ccr.2021.214086 214086.

Xu, H., Xu, J., Li, H., Zhang, W., Zhang, Y., Zhai, Z., 2022. Highly sensitive ethanol and acetone gas sensors with reduced working temperature based on Sr-doped $BiFeO_3$ nanomaterial. J. Mater. Res. Technol. 17, 1955–1963. https://doi.org/10.1016/j.jmrt.2022.01.137.

Yamazoe, N., Sakai, G., Shimanoe, K., 2003. Oxide semiconductor gas sensors. Catal. Surv. Asia 7, 63–75. https://doi.org/10.1023/A:1023436725457.

Yang, D.J., Kamienchick, I., Youn, D.Y., Rothschild, A., Kim, I.D., 2010. Ultrasensitive and highly selective gas sensors based on electrospun SnO_2 nanofibers modified by Pd loading. Adv. Funct. Mater. 20, 4258–4264. https://doi.org/10.1002/adfm.201001251.

Yu, W., Jiang, K., Wu, J., Gan, J., Zhu, M., Hu, Z., Chu, J., 2011. Electronic structures and excitonic transitions in nanocrystalline iron-doped tin dioxide diluted magnetic semiconductor films: an optical spectroscopic study. Phys. Chem. Chem. Phys. 13, 6211–6222. https://doi.org/10.1039/C0CP01503B.

Yu, Q., Zhang, Y., Xu, Y., 2021. Hierarchical hollow $BiFeO_3$ microcubes with enhanced acetone gas sensing performance. Dalton Trans. 50, 6702–6709. https://doi.org/10.1039/D1DT00532D.

Yuan, L., Hyodo, T., Shimizu, Y., Egashira, M., 2011. Preparation of mesoporous and/or macroporous SnO_2-based powders and their gas-sensing properties as thick film sensors. Sensors 11, 1261–1276. https://doi.org/10.3390/s110201261.

Zhang, J., Zhang, B., Yao, S., Li, H., Chen, C., Bala, H., Zhang, Z., 2022. Improved triethylamine sensing properties of fish-scale-like porous SnO_2 nanosheets by decorating with Ag nanoparticles. J. Materiomics 8, 518–525. https://doi.org/10.1016/j.jmat.2021.06.005.

Zheng, J., Hou, H., Fu, H., Gao, L., Liu, H., 2021. Size-controlled synthesis of porous $ZnSnO_3$ nanocubes for improving formaldehyde gas sensitivity. RSC Adv. 11, 20268–20277. https://doi.org/10.1039/D1RA01852C.

Zhong, X., Yang, B., Zhang, X., Jia, J., Yi, G., 2012. Effect of calcining temperature and time on the characteristics of Sb-doped SnO_2 nanoparticles synthesized by the sol–gel method. Particuology 10, 365–370. https://doi.org/10.1016/j.partic.2011.09.005.

Zhou, S., Wang, H., Hu, J., Lv, T., Rong, Q., Zhang, Y., Zi, B., Chen, M., Zhang, D., Wei, J., Zhang, J., Liu, Q., 2022. Formaldehyde gas sensor with extremely high response employing cobalt-doped SnO_2 ultrafine nanoparticles. Nanoscale Adv. 4, 824–836. https://doi.org/10.1039/D1NA00625H.